

FORMATION OF PRIMORDIAL SUPERMASSIVE STARS BY RAPID MASS ACCRETION

TAKASHI HOSOKAWA^{1,2}, HAROLD W. YORKE², KOHEI INAYOSHI³,
KAZUYUKI OMUKAI^{4,3}, NAOKI YOSHIDA^{1,5}

Draft version September 11, 2018

ABSTRACT

Supermassive stars (SMSs) forming via very rapid mass accretion ($\dot{M}_* \gtrsim 0.1 M_\odot \text{ yr}^{-1}$) could be precursors of supermassive black holes observed beyond redshift of about 6. Extending our previous work, we here study the evolution of primordial stars growing under such rapid mass accretion until the stellar mass reaches $10^{4-5} M_\odot$. Our stellar evolution calculations show that a star becomes supermassive while passing through the “supergiant protostar” stage, whereby the star has a very bloated envelope and a contracting inner core. The stellar radius increases monotonically with the stellar mass, until $\simeq 100 \text{ AU}$ for $M_* \gtrsim 10^4 M_\odot$, after which the star begins to slowly contract. Because of the large radius the effective temperature is always less than 10^4 K during rapid accretion. The accreting material is thus almost completely transparent to the stellar radiation. Only for $M_* \gtrsim 10^5 M_\odot$ can stellar UV feedback operate and disturb the mass accretion flow. We also examine the pulsation stability of accreting SMSs, showing that the pulsation-driven mass loss does not prevent stellar mass growth. Observational signatures of bloated SMSs should be detectable with future observational facilities such as the James Webb Space Telescope. Our results predict that an inner core of the accreting SMS should suffer from the general relativistic instability soon after the stellar mass exceeds $10^5 M_\odot$. An extremely massive black hole should form after the collapse of the inner core.

Subject headings: cosmology: theory – early universe – galaxies: formation – stars: formation – accretion

1. INTRODUCTION

Theoretical scenarios of forming supermassive black holes (SMBHs) confront the observations of bright quasars beyond redshift 6, which require that SMBHs exceeding $10^9 M_\odot$ form in less than 1 Gyr after the Big Bang (e.g., Treister et al. 2011; Mortlock et al. 2011). The direct collapse of supermassive stars (SMSs; $M_* \gtrsim 10^5 M_\odot$) could be a crucial first step leading to the rapid formation of SMBHs in the early universe. If an SMS were to form, its inevitable collapse into a very massive black hole would be initiated by the general relativistic (GR) instability (e.g., Iben 1963; Chandrasekhar 1964). The $\sim 10^5 M_\odot$ black holes thus generated could further grow via subsequent mass accretion and mergers (e.g., Haiman 2013, and references therein), and finally become the SMBHs powering young bright quasars (e.g., Johnson et al. 2013c).

The formation of an SMS should be understood in the context of primordial star formation (e.g., Bromm et al. 2009). Recent theoretical work investigates how massive such primordial stars are, studying the late evolutionary stage whereby a protostar grows in mass via mass accretion from a surrounding envelope (e.g.,

Omukai & Palla 2003; McKee & Tan 2008; Stacy et al. 2010; Hosokawa et al. 2011b, 2012b; Stacy et al. 2012; Susa 2013). Although the exact shape of their mass spectrum is still under debate, recent studies show that primordial stellar masses should be widely distributed from a few tens to hundreds of solar masses (e.g., Susa 2013; Hirano et al. 2013). It is likely that the first stars are normally less massive than $10^3 M_\odot$. However, SMSs with $M_* \gg 10^3 M_\odot$ could nevertheless form through a non-standard mode of primordial star formation, in analogy to the present-day formation of a massive star exceeding $100 M_\odot$, which although very rare, can form under non-standard initial conditions which differ from those for low-mass ($M_* \sim 1 M_\odot$) stars (e.g., Zinnecker & Yorke 2007).

A non-standard condition for forming the SMSs could be realized when the formation of H_2 molecules, the primary coolant in the primordial gas, is hindered in a massive dark halo (e.g., Bromm & Loeb 2003). A number of processes preventing H_2 formation have been proposed, e.g., photodissociation by strong UV background (Omukai 2001; Oh & Haiman 2002; Wise et al. 2008; Shang et al. 2010; Wolcott-Green et al. 2011; Inayoshi & Omukai 2011; Agarwal et al. 2012), and collisional dissociation in dense shocks (Inayoshi & Omukai 2012). Without H_2 molecules a primordial gas cloud collapses nearly isothermally at $T \simeq 8000 \text{ K}$ due to atomic hydrogen cooling. Numerical models suggest that one or more supermassive stars may form in either spherical infall or disks (e.g., Bromm & Loeb 2003; Regan & Haehnelt 2009; Latif et al. 2013a,b). After that, the stellar mass increases via very rapid mass accretion at $\dot{M}_* \sim 0.1 - 1 M_\odot \text{ yr}^{-1}$ (e.g., Latif et al. 2013a;

¹ Department of Physics and Research Center for the Early Universe, The University of Tokyo, Tokyo 113-0033, Japan; takashi.hosokawa@phys.s.u-tokyo.ac.jp, hosokwtk@gmail.com

² Jet Propulsion Laboratory, California Institute of Technology, Pasadena CA 91109, USA

³ Department of Physics, Kyoto University, Kyoto 606-8502, Japan

⁴ Astronomical Institute, Tohoku University, Sendai 980-8578, Japan

⁵ Kavli Institute for the Physics and Mathematics of the Universe, University of Tokyo, Kashiwa, Chiba 277-8583, Japan

Choi et al. 2013). The star can become supermassive within 10^6 yr with such rapid mass accretion. Note this process is operative only in an almost pristine gas with metallicity $\lesssim 10^{-5} Z_{\odot}$, since fragmentation induced by dust cooling would prohibit the monolithic collapse of massive clouds at higher metallicities (Omukai et al. 2008).

The evolution of accreting SMSs is critical for understanding their formation process. For instance, the stellar effective temperature controls energies of photons emitted by an SMS, whose luminosity could exceed $10^9 L_{\odot}$ at $M_* \sim 10^5 M_{\odot}$. If the SMS emits a copious amount of UV photons, an HII region should form around the SMS. Johnson et al. (2012) show that, under spherical symmetry, the resulting UV feedback halts the mass accretion only for $M_* \gtrsim 10^6 M_{\odot}$. In disk geometries, however, a bipolar HII region should emerge and strong UV feedback could limit mass accretion much earlier, as expected in the standard cases of primordial star formation (e.g., McKee & Tan 2008; Hosokawa et al. 2011b; Stacy et al. 2012; Susa 2013). The final mass of the SMS should depend on the details of its evolution before the rapid mass accretion ceases.

The evolution of SMSs with various metallicities has been modeled in detail (e.g., Osaki 1966; Unno 1971; Appenzeller & Fricke 1972a,b; Fricke 1973; Fuller et al. 1986). However, they do not consider the formation stage with rapid mass accretion, which could significantly change the stellar structure (e.g., Begelman 2010; Hosokawa et al. 2012a; Schleicher et al. 2013). The ultimate fate of an SMS, i.e., whether a star collapses to form a BH (e.g., Shibata & Shapiro 2002; Montero et al. 2012; Reisswig et al. 2013), explodes by thermo-nuclear burning (e.g., Whalen et al. 2012; Johnson et al. 2013b; Whalen et al. 2013a,b), or evolves into a “quasi-star” (Begelman et al. 2008), also depends on the mass accretion history during the formation stage.

Hosokawa et al. (2012a, hereafter HOY12) study stellar evolution with very high accretion rates $\dot{M}_* \gtrsim 10^{-2} M_{\odot} \text{ yr}^{-1}$, employing numerical codes developed in our previous work (e.g., Omukai & Palla 2003; Hosokawa & Omukai 2009; Hosokawa et al. 2010). Our calculations show that the evolution at such high accretion rates qualitatively differs from that with lower accretion $\dot{M}_* \lesssim 10^{-2} M_{\odot} \text{ yr}^{-1}$, normally expected for primordial star formation. At high accretion rates the stellar radius is found to increase monotonically with mass

$$R_* \simeq 2.6 \times 10^3 R_{\odot} \left(\frac{M_*}{100 M_{\odot}} \right)^{1/2} \quad (1)$$

for $M_* \gtrsim 100 M_{\odot}$, independent of the accretion rate. The stellar effective temperature is almost constant at $\simeq 5000$ K during this stage, and the resulting stellar UV luminosity is very low. However, HOY12 could only focus on the early evolution up to stellar masses of $10^3 M_{\odot}$, because their iteration procedure for constructing stellar models converged very slowly at higher masses. Here, using a different stellar evolution code (Yorke & Bodenheimer 2008), we extend the previous work of HOY12 and discuss the evolution up to stellar masses $10^{4-5} M_{\odot}$. Moreover, we consider the pulsation stability of accreting SMSs extending Inayoshi et al.

(2013a, hereafter IHO13), whose analyses are limited to $M_* \leq 10^3 M_{\odot}$. We examine whether the resulting mass loss could limit stellar growth via rapid mass accretion.

This paper is organized as follows. First, we briefly describe the numerical methods adopted and cases considered in Section 2. The results are presented in Section 3 and compared with our previous work in HOY12. We provide discussions and concluding remarks in Sections 4 and 5.

2. NUMERICAL MODELING OF ACCRETING STARS

2.1. Evolutionary Calculations

We study the evolution of rapidly accreting stars by numerically solving their interior structure. The governing equations are the usual stellar structure equations including effects of the mass accretion (e.g., Kippenhahn & Meyer-Hofmeister 1977; Stahler et al. 1980). In this paper, we employ the numerical code developed by Yorke & Bodenheimer (2008), where the Henyey method (Henyey et al. 1964) is employed to solve the stellar interior structure (also see Bodenheimer et al. 2007). The outer boundary conditions for the interior are provided by solving the structure of a gray atmosphere. To do this, we integrate inward the equations of hydrostatic equilibrium and radiative or convective transfer over the atmosphere with a Runge-Kutta procedure. The stellar effective temperature T_{eff} is defined at the optical depth $\tau = 2/3$ measured from the exterior. The atmosphere integration extends to a connecting point at a temperature $T_{\text{atm}} \simeq \text{several} \times T_{\text{eff}}$, which varies slowly with time. We presume that the thermal state of the accreting material is the same as in the outer atmosphere (see below). The material added to the atmosphere is ultimately incorporated into the interior by means of an automatic rezoning procedure.

The current numerical code differs from that used in HOY12 (also see Hosokawa & Omukai 2009), where the same governing equations were solved by a shooting method instead of the Henyey method used here. Inside an SMS radiation dominates the total pressure, but a small contribution by the gas is crucial in determining its structure such as the radius. Here we adopt the gas pressure as one of our independent Henyey variables in place of the total pressure. This enables us to accurately solve the structure of a SMS. The outer boundary conditions are also different. Most of the cases examined in HOY12 assume spherical accretion onto a star (e.g., Stahler et al. 1980; Hosokawa & Omukai 2009), whereby steady accretion flow hits the stellar surface forming an accretion shock front. In this case, we also consider the structure of the steady accretion flow falling onto the star. We calculate the radial structure of both the outer accretion flow and stellar interior for satisfying the shock jump conditions.

HOY12 also study a few cases with a different outer boundary, the photospheric boundary conditions:

$$P_{\text{surf}} = \frac{2}{3} \frac{1}{\kappa_{\text{surf}}} \frac{GM_*}{R_*^2}, \quad (2)$$

and

$$L_* = 4\pi R_*^2 \sigma T_{\text{surf}}^4 \quad (3)$$

(e.g., Palla & Stahler 1992; Hosokawa et al. 2010), where the suffix “surf” represents quantities at the stellar sur-

face and σ is the Stefan-Boltzmann constant. This boundary is rather similar to that adopted in the current code, except that the structure of the atmosphere is not solved. These outer boundary conditions assume that the accreting material is added to the star through a geometrically thin disk, whereby most of the stellar surface can still freely radiate (no backwarming).

Although one can see that the photospheric boundary is realistic for the assumed disk accretion, it is important that the outer boundary condition correctly determines the specific entropy of accreting material (e.g., Hartmann et al. 1997; Hosokawa et al. 2011a). With the photospheric boundary, the accreting material has the smallest amount of entropy (so-called *cold accretion*), which is the value at the stellar surface. In this case, accreting gas would slowly approach the star through the disk, radiating its heat away before reaching the stellar surface. The accreting gas gently lands on the stellar surface with the same entropy as in the outer photosphere. With the spherically symmetric shock boundary condition, on the other hand, the accreting material has a much higher entropy than for the cold accretion case, carrying a larger fraction of the entropy generated in the shock front into the stellar interior. However, even for the case of highly non-spherical accretion through a circumstellar disk, the very rapid mass accretion considered here means that a non-negligible amount of entropy should be advected into the star. For this reason, HOY12 adopt the shock boundary condition for the fiducial cases.

Detailed modeling of the thermal properties of the accretion flow is beyond the scope of spherically symmetric stellar evolution calculations. Realizing that a fraction of the gravitational energy released by the accreting gas will be deposited into the stellar interior (e.g., Siess & Forestini 1996; Siess et al. 1997), we add an additional luminosity

$$L_{*,\text{acc}} \equiv \eta L_{\text{acc}} = \eta \frac{GM_* \dot{M}_*}{R_*} \quad (4)$$

to the bottom of the atmosphere. The fraction of the deposited accretion luminosity η is treated as a free parameter with a value $0 \leq \eta \leq 1$. The limit of cold accretion corresponds to $\eta = 0$. More detailed modeling would be possible if we were to consider how the deposited energy is spatially distributed in the stellar interior (e.g., Siess & Forestini 1996), i.e. not only at the bottom of the atmosphere. However, we find that the evolution does not depend on η for $M_* \gtrsim 100 M_\odot$.

2.2. Cases Considered

Table 1 summarizes the cases considered in this paper. We follow the stellar evolution with rapid mass accretion at various constant rates of 0.01, 0.1, 0.3, and $1.0 M_\odot \text{ yr}^{-1}$ beginning with a $2 M_\odot$ initial model. Cases with different values of η are also examined for each accretion rate. Although the current numerical code enables following the evolution far beyond that considered by HOY12, we ultimately encounter numerical convergence difficulties. Here we present the evolution for $\simeq 10^5$ years in each case. The stellar mass reaches $10^5 M_\odot$ with the accretion rate $\dot{M}_* = 1.0 M_\odot \text{ yr}^{-1}$ (cases a1, see table 1).

The cases with the lowest accretion rate of

Table 1. Cases Considered

Cases	\dot{M}_* ($M_\odot \text{ yr}^{-1}$)	η	$M_{*,f}$ (M_\odot)
a1-e0	1.0	0.0	10^5
a1-e0.01	1.0	0.01	10^5
a1-e0.1	1.0	0.1	10^5
a1-e1	1.0	1.0	10^5
a0.3-e0.1	0.3	0.1	6×10^4
a0.1-e0	0.1	0.0	2×10^4
a0.1-e0.01	0.1	0.01	2×10^4
a0.1-e0.1	0.1	0.1	2×10^4
a0.1-e1	0.1	1.0	2×10^4
a0.01-e0.1	0.01	0.1	2×10^3
a0.01-e0	0.01	0.0	2×10^3

Col. 2: mass accretion rate, Col. 3: fraction of the accretion luminosity deposited in the stellar interior (see eq. 4), Col. 4: final stellar mass.

$0.01 M_\odot \text{ yr}^{-1}$ (cases a0.01) are relevant to the normal mode of the primordial star formation, where H_2 molecular cooling operates. We also study these cases as our previous calculations predict that, with such moderately high accretion rates, the stellar radius shows a peculiar behavior, oscillating with increasing stellar mass (e.g., Omukai & Palla 2001, 2003, HOY12). Below, we show that our current numerical code also provides a similar evolution despite a number of differences, e.g., the outer boundary conditions.

3. RESULTS

3.1. Evolution of Rapidly Accreting Supermassive Stars

3.1.1. Outline of the Evolution

Figure 1 presents the overall stellar evolution with the accretion rates $\dot{M}_* = 0.1 M_\odot \text{ yr}^{-1}$ (case a0.1-e0.1) and $1.0 M_\odot \text{ yr}^{-1}$ (case a1-e0.1), where the deposited energy fraction η is set at 0.1. We see that, in both cases, the early evolution of the stellar radius agrees well with our previous results for $M_* \lesssim 10^3 M_\odot$ (HOY12). The small deviations for $M_* \lesssim 100 M_\odot$ are mostly due to the different outer boundary conditions as explained in Sec. 2.1 (also see Sec. 3.1.4 below). Our current results show that the star continues to expand for $M_* \gtrsim 10^3 M_\odot$. The stellar radius increases monotonically with mass according to relation (1) for $100 M_\odot \lesssim M_* \lesssim 10^4 M_\odot$, and finally begins to decrease for $M_* \gtrsim 3 \times 10^4 M_\odot$. Nonetheless, the stellar radius remains very large at $R_* \simeq 2 \times 10^4 R_\odot \simeq 100 \text{ AU}$. With the accretion rate of $\dot{M}_* = 1.0 M_\odot \text{ yr}^{-1}$, we obtain an accreting $10^5 M_\odot$ star which is still significantly bloated.

To understand why the radius begins to decrease for $M_* \gtrsim 10^4 M_\odot$, it is helpful to recall how equation (1) is derived (also see HOY12). In general, the luminosity of very massive stars is close to the Eddington value,

$$L_* = 4\pi R_*^2 \sigma T_{\text{eff}}^4 \simeq L_{\text{Edd}} \propto M_* \quad (5)$$

Because of the very strong temperature-dependence of gas opacity with H^- bound-free absorption, which dominates near the stellar surface, the effective temperature is locked at several $\times 10^3 \text{ K}$ (e.g., Hayashi 1961). Equation (1) is derived by substituting $T_{\text{eff}} = 5000 \text{ K}$ into (5). The upper panel of Figure 1 also shows that the effective temperature is certainly locked at $\simeq 5000 \text{ K}$ for $M_* \lesssim 10^4 M_\odot$. However, we see that the effective temperature gradually increases for $M_* \gtrsim 10^4 M_\odot$, when

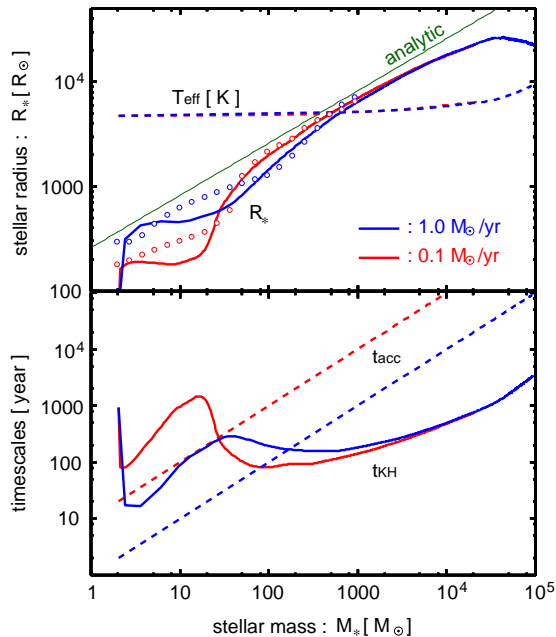


FIG. 1.— Protostellar evolution over $\sim 10^5$ years with accretion rates $\dot{M}_* = 0.1 M_\odot \text{ yr}^{-1}$ (case a0.1-e0.1, red lines) and $1.0 M_\odot \text{ yr}^{-1}$ (case a1-e0.1, blue lines), and $\eta = 0.1$ (see text). *Upper panel:* evolution of the stellar radius (solid lines). The open circles represent our previous results taken from Hosokawa et al. (2012a) for $M_* \lesssim 10^3 M_\odot$ with $\dot{M}_* = 0.1 M_\odot \text{ yr}^{-1}$ (red) and $1.0 M_\odot \text{ yr}^{-1}$ (blue). The thin green line shows the analytic mass-radius relation given by equation (1). The evolution of the stellar effective temperature is also overlaid on the above plots (dashed lines), using the same scale as for the stellar radius. *Lower panel:* evolution of the accretion timescale (dashed lines) and Kelvin-Helmholtz timescale (solid lines).

the stellar expansion ceases. The deviation of the stellar expansion from relation (1) is due to the rise of effective temperature, which is separately considered in Sec. 3.1.3 below.

In general, the evolution of an accreting star can be understood by comparing the accretion time

$$t_{\text{acc}} \equiv \frac{M_*}{\dot{M}_*}, \quad (6)$$

the timescale for stellar mass growth, to the Kelvin-Helmholtz (KH) time

$$t_{\text{KH}} \equiv \frac{GM_*^2}{R_* L_*}, \quad (7)$$

over which the star radiates away its gravitational energy (e.g., Stahler et al. 1986). The lower panel of Figure 1 shows that the balance between these two timescales is inverted from $t_{\text{KH}} > t_{\text{acc}}$ to $t_{\text{KH}} < t_{\text{acc}}$ during the evolution, e.g., at $M_* \simeq 200 M_\odot$ for $1.0 M_\odot \text{ yr}^{-1}$. As explained in the literature (e.g., Omukai & Palla 2003; Hosokawa & Omukai 2009), this is because the KH timescale decreases as the stellar luminosity L_* rapidly increases with stellar mass. The same timescale inversion is also shown in HOY12 (see their Fig. 3).

We see that the accreting stars have a very short KH timescale compared to the accretion timescale for $M_* \gtrsim$ a few $\times 10^2 M_\odot$. This means that the star efficiently loses its energy via radiation, which usually leads

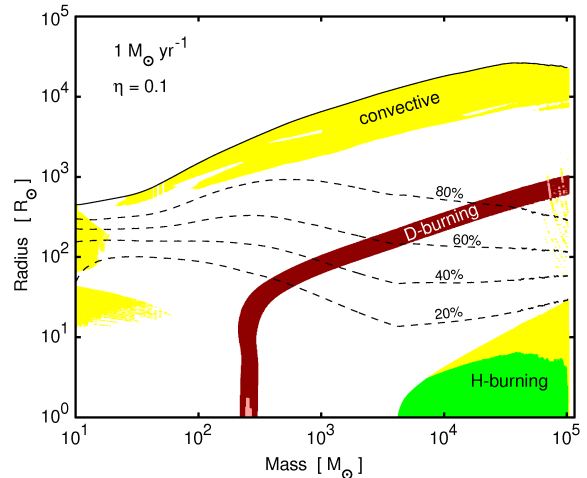


FIG. 2.— Evolution of the stellar interior structure until the accreted stellar mass reaches $10^5 M_\odot$ for the accretion rate $\dot{M}_* = 1 M_\odot \text{ yr}^{-1}$ and energy fraction $\eta = 0.1$ (case a1-e0.1). The black solid and dashed lines represent the radial positions of the stellar surface and mass coordinates of 80%, 60%, 40%, and 20% of the total stellar mass in descending order. The white and yellow areas represent radiative and convective zones without nuclear fusion, respectively. The brown stripe denotes the radiative layer where deuterium burning occurs, i.e., the energy production rate exceeds the mass-averaged steady rate with mass accretion $L_{\text{D,st}}/\dot{M}_*$ (see equation 8). The green area represents a convective core where hydrogen burning occurs, i.e., the hydrogen depletion timescale is shorter than the lifetime of the main-sequence star with the same mass. Pink zones depict convective deuterium burning.

to contraction (so-called KH contraction). However, our results show that the stellar radius continues to increase until $M_* \gtrsim 3 \times 10^4 M_\odot$. This suggests that the star has a very inhomogeneous structure, e.g., most of the stellar interior contracts while radiating energy away, whereas a surface layer expands as it receives part of the outward heat flux. HOY12 show this core-envelope structure of rapidly accreting stars for $M_* \leq 10^3 M_\odot$. In Sec. 3.1.2 below, we show that the same stellar structure is maintained even after the star becomes supermassive, $M_* \gtrsim 10^4 M_\odot$.

3.1.2. Stellar Interior Structure

We here investigate the evolution of the interior structure of accreting supermassive stars. Figure 2 shows the evolution with the accretion rate $\dot{M}_* = 1.0 M_\odot \text{ yr}^{-1}$ and input energy fraction $\eta = 0.1$ (case a1-e0.1). As explained in Sec. 3.1.1, the KH timescale falls below the accretion time at $M_* \simeq 200 M_\odot$ in this case.

Although deuterium burning begins soon after the timescale inversion, this hardly influences the subsequent evolution (also see HOY12). At this stage deuterium burns at nearly a steady rate, because it is replenished by accretion as quickly as consumed by burning,

$$L_{\text{D,st}} \equiv \dot{M}_* \delta_{\text{D}} = 1.5 \times 10^6 L_\odot \left(\frac{\dot{M}_*}{1 M_\odot \text{ yr}^{-1}} \right) \left(\frac{[\text{D}/\text{H}]}{2.5 \times 10^{-5}} \right), \quad (8)$$

where δ_{D} is the energy produced via deuterium burning per unit mass. The energy released by deuterium burning is negligible in comparison to the local luminosity, approximately given by the Eddington value. The heat

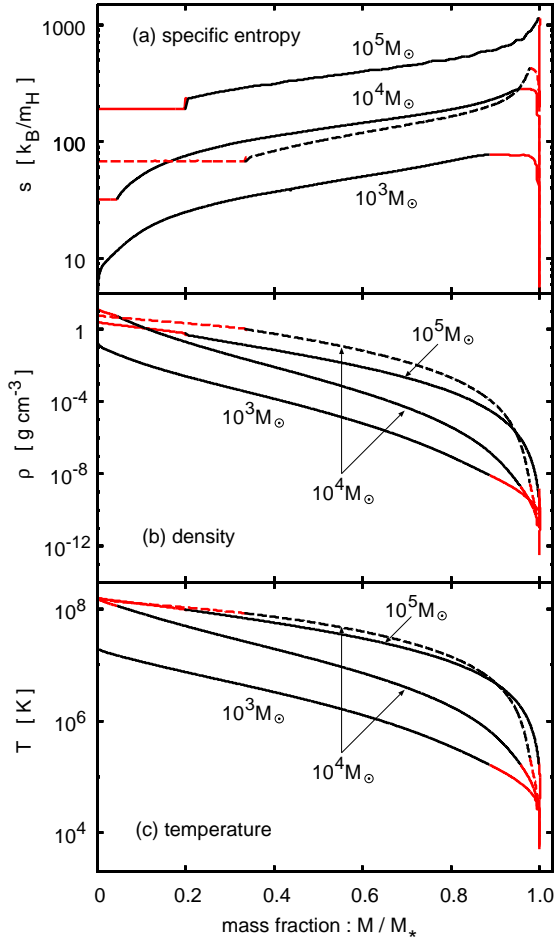


FIG. 3.— Snapshots of the thermal and density structure in the stellar interior. The solid and dashed lines represent the two accretion rates $1.0 M_{\odot} \text{ yr}^{-1}$ and $0.1 M_{\odot} \text{ yr}^{-1}$ with the same input energy fraction $\eta = 0.1$ (cases a1-e0.1 and a0.1-e0.1). The panels (a), (b), and (c) show the radial distributions of the specific entropy, density, and temperature as functions of the normalized mass coordinate M/M_* . For the accretion rate $1.0 M_{\odot} \text{ yr}^{-1}$ the structure after $10^3 M_{\odot}$, $10^4 M_{\odot}$, and $10^5 M_{\odot}$ have accreted is displayed. Profiles at the lower accretion rate are shown only for the $10^4 M_{\odot}$ star. The red parts denote the convective layers.

generated by nuclear fusion is rapidly transported via radiation without causing convection. This is not the case with extremely cold mass accretion, $\eta = 0$ (see below).

Figure 2 shows that for $M_* \gtrsim 200 M_{\odot}$ the star has an inhomogeneous mass distribution; a surface layer which contains only a tiny fraction of the total stellar mass significantly inflates. Moreover, we see that the star becomes increasingly centrally condensed as the stellar mass increases. This is because most of the stellar interior is contracting in this stage as explained in Sec. 3.1.1. The gravitational energy released by the contracting interior is radiatively transported outward. However, part of the outward flux is absorbed in a surface layer where the opacity is higher than in the interior. As a result, the surface layer has a high specific entropy and largely inflates. Figure 2 shows that the energy is partly transported by convection in this semi-opaque surface layer. Figure 3-(a) presents the characteristic profiles of the specific entropy in the stellar interior, showing that the entropy increases outward to reach a maximum at the bottom of the sur-

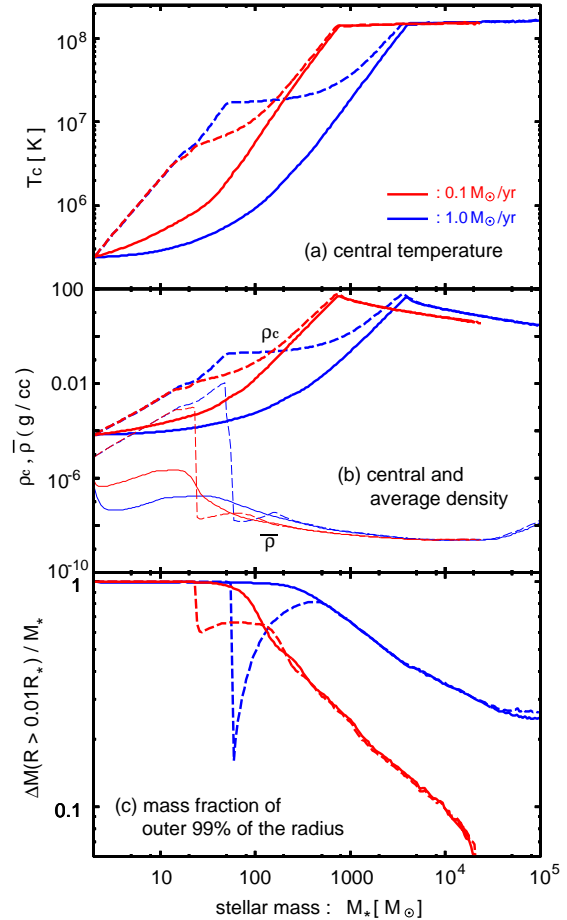


FIG. 4.— Variations of the stellar interior structure with different accretion rates M_* and input energy fractions η . The panels (a), (b), and (c) show the evolution of the central temperature T_c , the central density ρ_c , the average density $\bar{\rho}$, and the mass fraction of an outer layer which covers 99 % of the stellar radius $\Delta M(R > 0.01 R_*)/M_*$. The blue and red colors denote the different accretion rates $1.0 M_{\odot} \text{ yr}^{-1}$ and $0.1 M_{\odot} \text{ yr}^{-1}$, respectively. The solid and dashed lines represent deposited energy fractions of $\eta = 0.1$ (cases a1-e0.1 and a0.1-e0) and 0.0 (cases a0.1-e0.1 and a0.1-e0).

face convective layer.

Figure 4-(a) shows that, as in the ordinary KH contraction stage, the stellar central temperature increases with mass. Hydrogen burning begins at $M_* \simeq 4 \times 10^3 M_{\odot}$, after which the central temperature is fixed at $\simeq 1.5 \times 10^8 \text{ K}$ by the thermostat effect due to the strong temperature-dependence of energy production through the CNO cycle. Although initially at zero metallicity a small amount of carbon is produced in the center through the $3\text{-}\alpha$ process during KH contraction, which allows efficient hydrogen nuclear burning via the CNO cycle. Figures 2 and 4 show that a convective hydrogen-burning core grows with increasing stellar mass. The ignition of hydrogen burning halts the KH contraction within and near the convective core. In fact, Figure 4-(b) shows that the ratio of the central density to the average density decreases with increasing mass after hydrogen burning begins. However, most of the stellar interior is still contracting as can be inferred from Figure 2. As the mass increases from $10^4 M_{\odot}$

to $10^5 M_\odot$ the radii of 80% and 60% of the total mass continue to decrease and the radii of 40% and 20% increase only slightly, but much less than the growth in mass. Finally, at $M_* \simeq 10^5 M_\odot$ the outer 99 % of the star in radius contains only 25 % of its total mass (see Figure 4-(c)). Figure 3-(b) and (c) show that the average interior density and temperature still rise with increasing stellar mass as a result of the on-going contraction for $M_* \gtrsim 10^4 M_\odot$. The gravitational energy released by the contracting envelope compensates most of the stellar surface luminosity, even after the ignition of hydrogen burning. Most of the heat generated by nuclear fusion is absorbed in the convective core, whose entropy is consequently elevated as shown in Figure 4-(a).

Finally, we consider how the above evolution changes with a lower accretion rate $\dot{M}_* = 0.1 M_\odot \text{ yr}^{-1}$. As can be inferred from Figure 1, the evolution is qualitatively the same as in the previously discussed cases with $\dot{M}_* = 1.0 M_\odot \text{ yr}^{-1}$. There is a quantitative difference, however. At the lower accretion rate the accretion timescale is correspondingly much longer than the KH timescale for $M_* \gtrsim 100 M_\odot$. The star has a more centrally-concentrated mass distribution for a given stellar mass, because it has had more time to contract and has radiated more energy $\int L_* dt$, which has to be covered by gravitational contraction. Figure 4-(a) shows that, as a result, the central temperature is higher at comparable stellar masses, so that hydrogen burning begins before the stellar mass reaches $10^3 M_\odot$. The outer envelope of the star still continues to contract after the ignition of hydrogen as previously described. Figure 3-(b) and (c) show that, for a $10^4 M_\odot$ star, the average interior temperature and density for $\dot{M}_* = 0.1 M_\odot \text{ yr}^{-1}$ are much higher than those with $\dot{M}_* = 1.0 M_\odot \text{ yr}^{-1}$. It is interesting that, regardless of the different interior structure, the evolution of the stellar radius, while obeying relation (1), is almost independent of the accretion rate.

3.1.3. Stellar Surface Structure and Termination of the Expansion

Our results show that rapidly accreting SMSs have a large radius ~ 100 AU, even after the stellar mass exceeds $10^4 M_\odot$. However, the stellar expansion gradually slows down, no longer following the analytic mass-radius relation (1). Figure 1 shows that, especially with $\dot{M}_* = 1.0 M_\odot \text{ yr}^{-1}$, the stellar radius finally turns around and decreases slightly for $M_* \gtrsim 3 \times 10^4 M_\odot$. Here we consider why the stellar expansion finally ceases.

As explained in Sec. 3.1.2, the stellar structure is not homogeneous during expansion. Only a surface layer which has a tiny fraction of the total stellar mass inflates. Whereas most of the stellar interior contracts and radiates the energy away, the outer layer absorbs a part of the outward flux and gains a relatively high specific entropy, resulting in the surface-layer bloating. The physical state of the outermost part of a star is thus key to understand the termination of the expansion. Figure 5 presents several snapshots of the outermost radial profiles of pressure, density, and opacity as functions of the interior temperature T for case a1-e0.1 ($\dot{M}_* = 1.0 M_\odot \text{ yr}^{-1}$ and $\eta = 0.1$). Note that higher interior temperatures represent deeper stellar layers, because the interior temperature increases

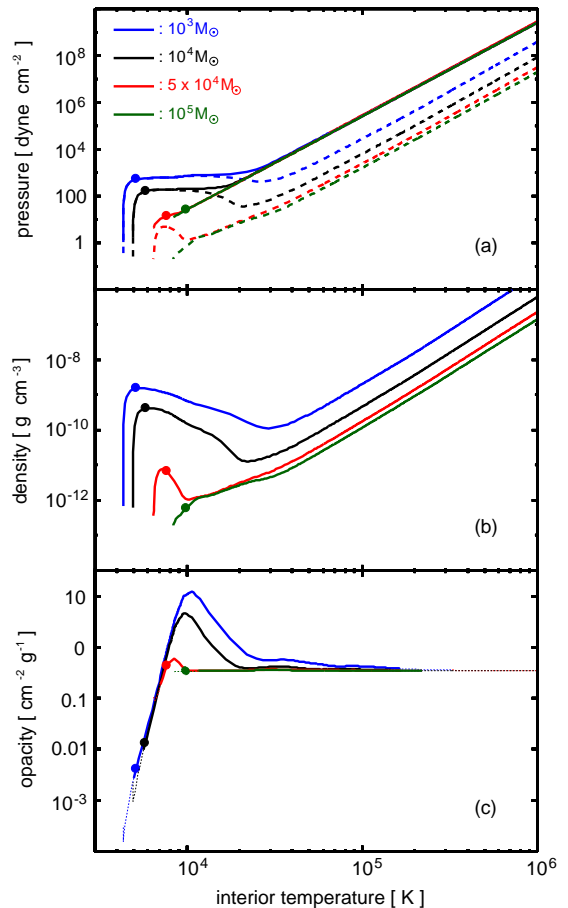


FIG. 5.— Structure near the stellar surface for the accretion rate $\dot{M}_* = 1 M_\odot \text{ yr}^{-1}$ and input energy fraction $\eta = 0.1$ (case a1-e0.1). The panels (a), (b), and (c) show the radial distributions of pressure, density and opacity as functions of the interior temperature. Higher interior temperatures correspond to greater depths into the star. The different colors denote the different epochs when the stellar mass is $10^3 M_\odot$ (blue), $10^4 M_\odot$ (black), $5 \times 10^4 M_\odot$ (red), and $10^5 M_\odot$ (green). The filled circles on the lines mark the positions of the photosphere. In panel (a), the solid and dashed lines represent the total pressure and gas pressure, respectively. In panel (c), the solid and thin dotted lines denote the convective and radiative layers, respectively. For $T \gtrsim 10^5$ K the opacity converges to the constant value from Thomson scattering.

monotonically toward the center. For $M_* \lesssim 10^4 M_\odot$ while the stellar radius is still increasing with mass according to (1), the star has a characteristic feature for $T \lesssim 3 \times 10^4$ K. Panel (a) shows that the gas pressure dominates over the radiation pressure there, shaping the almost flat profile within the photosphere. We also see that the density accordingly *increases* outward (panel-b), i.e. it is not monotonic. This structure is called a density inversion. Such density inversions occasionally occur in the outermost layers where the radiative flux locally exceeds the Eddington value. The hydrostatic balance is achieved with the inward gas pressure gradient (around $T \simeq 2 \times 10^4$ K in panel-a), which helps gravity balance the outward radiation force. The gas opacity has a peak at $T \simeq 10^4$ K because of the bound-free absorption of H and H^- (e.g., Kippenhahn et al. 2013). In the outer layers where $T \lesssim 10^4$ K, the opacity drops sharply with decreasing temperature, a general feature of H^- absorption, because at lower temperatures there are fewer free

electrons available for forming H^- ions.

However, this characteristic feature at the surface changes when the stellar mass exceeds $M_* > 10^4 M_\odot$. Radiation pressure starts to dominate the total pressure everywhere in the interior, and the density inversion almost disappears by the epoch of $M_* \simeq 10^5 M_\odot$. This behavior is due to the density-dependence of gas opacity. Figure 5-(c) shows that, at the low density $\rho \lesssim 10^{-11} \text{ g cm}^{-3}$, opacity in the surface layers drops to the Thomson scattering value as H^- absorption becomes inefficient (also see, e.g., Mayer & Duschl 2005). This is inevitable because collisional events between neutral hydrogen atoms and free electrons are required to form H^- ions and the H^- opacity is therefore proportional to $n_{\text{H}} n_{\text{e}}$.

Recall that equation (1) is derived assuming that the effective temperature is locked at $T_{\text{eff}} \simeq 5000 \text{ K}$ because of the strong temperature-dependence of H^- opacity. At the point when H^- ions no longer dominate the opacity in surface layers, these surface layers no longer efficiently absorb the heat flux coming from the contracting interior. We thus predict that the stellar radius will continue to decrease after the stellar mass exceeds $10^5 M_\odot$, in contrast to analytical considerations by Schleicher et al. (2013), who do not consider the detailed structure in the outermost part of the star where H^- opacity is important. We stress that the density-dependence of H^- opacity is a key for understanding the termination of the stellar expansion.

3.1.4. Evolution with Different Input Energy Fractions η

As described in Sec. 2.1, we parametrize the gravitational energy deposited into the stellar interior with the free parameter η . Here, we investigate how the stellar evolution varies with different values of η . We naively expect that, at a fixed stellar mass, the stellar radius would be larger with higher η , as the specific entropy of accreting materials would be enhanced. Figure 6 shows this is true only for early evolutionary stages when $M_* \lesssim 200 M_\odot$ ($30 M_\odot$) for the accretion rate $\dot{M}_* = 1.0 M_\odot \text{ yr}^{-1}$ ($0.1 M_\odot \text{ yr}^{-1}$, respectively), which corresponds to the epoch when the accretion timescale is shorter than the KH timescale (see Sec. 3.1.1). With this timescale imbalance, gas in the stellar interior retains the entropy originally obtained when accreted (Stahler et al. 1986), which in our case is determined by η . Differences of η thus influence the stellar structure during this stage. After the timescale inversion to $t_{\text{acc}} > t_{\text{KH}}$, the accretion luminosity L_{acc} becomes much smaller than the stellar luminosity L_* . Note that the timescale ratio $t_{\text{acc}}/t_{\text{KH}}$ is equal to the luminosity ratio L_*/L_{acc} by definition. The additional heat input into the atmosphere ηL_{acc} is thus negligible.

We find that the previous results of HOY12 with the shock boundary condition are similar to the current cases with $\eta = 0.1$. For the shock outer boundary, the specific entropy of accreting material is determined by solving the flow structure across the accretion shock front satisfying jump conditions (e.g., Stahler et al. 1980). We have no free parameters in this case. For the cold-accretion limit with $\eta = 0$, the stellar radius initially decreases with increasing stellar mass, until the star abruptly expands, e.g., at $M_* \simeq 50 M_\odot$ for $\dot{M}_* = 1 M_\odot \text{ yr}^{-1}$. HOY12 also

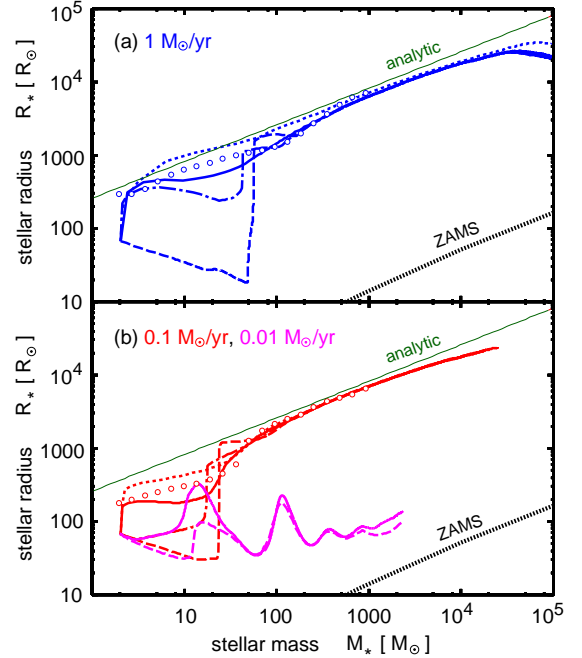


FIG. 6.— Evolution of the stellar radius with different fractions of the accretion luminosity deposited in the stellar interior, η . The upper and lower panels show the evolution with the accretion rates $\dot{M}_* = 1.0 M_\odot \text{ yr}^{-1}$, $0.1 M_\odot \text{ yr}^{-1}$, and $0.01 M_\odot \text{ yr}^{-1}$. The dotted, solid, dot-dashed, and dashed lines represent $\eta = 1.0$ (cases a1-e1 and a0.1-e1), 0.1 (a1-e0.1, a0.1-e0.1, and a0.01-e0.1), 0.01 (a1-e0.01 and a0.1-e0.01), and 0.0 (a1-e0, a0.1-e0, and a0.01-e0). In each panel, the thin green line shows the analytic mass-radius relation given by equation (1). The open circles denote our previous results taken from Hosokawa et al. (2012a) as in Figure 1. The black dotted line represents the mass-radius relation of ZAMS stars.

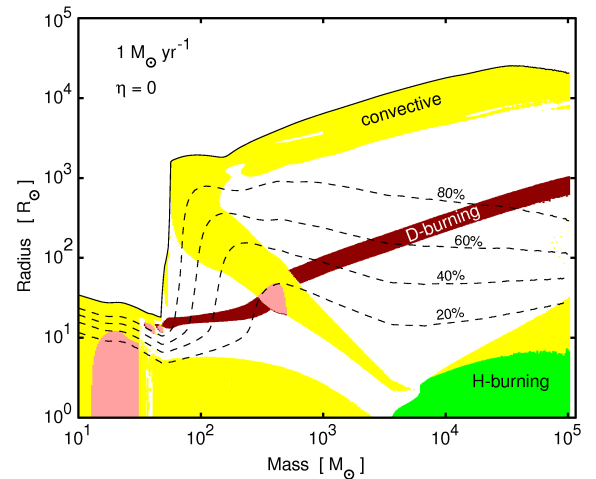


FIG. 7.— Same as Figure 2 but for the zero energy input $\eta = 0$ (case a1-e0).

find similar evolutionary behavior with the photospheric boundary conditions (2) and (3). This abrupt expansion in the cold-accretion limit is related to the extension of a deuterium-burning layer in the stellar interior, which is studied in detail in Hosokawa et al. (2010). We shall also examine the interior structure in the context of the current results in Sec. 3.1.2.

The lower panel of Figure 6 depicts the evolution of stellar radius at the lowest accretion rate considered here $\dot{M}_* = 10^{-2} M_\odot \text{ yr}^{-1}$ with the input energy fractions $\eta = 0.1$ and 0.0 (cases a0.01-e0.1 and a0.01-e0). In these cases, the timescale inversion to $t_{\text{KH}} < t_{\text{acc}}$ occurs around the first local maximum of the radius at $M_* \simeq 15 M_\odot$. The star contracts for a while after this point, radiating the energy away (KH contraction). As briefly mentioned in Sec. 2.2, however, we see a peculiar evolution for $M_* \gtrsim 100 M_\odot$, whereby the stellar radius slowly oscillates as the stellar mass increases. Omukai & Palla (2003) show that a similar evolution occurs with $\dot{M}_* \gtrsim 4 \times 10^{-3} M_\odot \text{ yr}^{-1}$ as the total stellar luminosity $L_{\text{tot}} \equiv L_* + L_{\text{acc}}$ approaches the Eddington value during the KH contraction. Whereas Omukai & Palla (2003) only show this evolution for shock outer boundary conditions, we show here that this oscillatory behavior occurs even in the extreme case of cold accretion, $\eta = 0$. Our results suggest that this characteristic evolutionary stage should emerge only with the moderately high accretion rates $\dot{M}_* \sim 10^{-2} M_\odot \text{ yr}^{-1}$, regardless of different thermal properties of the mass accretion.

The evolution of the interior structure differs significantly when the mass accretion is extremely cold. Figure 7 shows the evolution of the stellar interior structure for the extreme case of an input energy fraction $\eta = 0$ but with the same accretion rate (case a1-e0). The evolution of stellar structure deviates strongly from the case shown in Figure 2, particularly in the early stages for $M_* \lesssim 100 M_\odot$. Cold mass accretion leads to a much lower average entropy in the stellar interior, which results in a smaller stellar radius for $M_* \lesssim 30 M_\odot$. The central temperature is higher with the smaller radius for a given stellar mass, as shown in Figure 4-(a); the central temperature exceeds 10^6 K before the stellar mass reaches $10 M_\odot$. Deuterium burning begins much earlier than in the case with $\eta = 0.1$, even before the timescale inversion due to decreasing opacity in the stellar interior (see Sec. 3.1.1 above). Figure 2 also shows that the protostar is fully convective in this early stage, as the energy produced in the nearly opaque interior is transported mostly via convection.

Convective mixing transports the recently accreted deuterium inward to the stellar center, where nuclear fusion takes place. Central deuterium burning ceases soon after a radiative layer emerges in the stellar interior, which prevents convective mixing (this is a so-called radiative barrier, e.g., Palla & Stahler 1992). Deuterium burning resumes at the bottom of the surface convective layer, when the local temperature exceeds 1.5×10^6 K. Deuterium shell burning injects heat near the surface, which causes the surface layer to abruptly inflate at $M_* \simeq 50 M_\odot$ ¹. The later evolution for $M_* \gtrsim 10^3 M_\odot$, in particular, looks similar to the fiducial case shown in Figure 2. The evolution of accreting supermassive stars is thus insensitive to potential variations of the thermal efficiency of mass accretion, which is modeled with varying η in this paper.

¹ Similar behavior was found in our previous work Hosokawa et al. (2010), when we followed the evolution of present-day massive ($M_* \gtrsim 10 M_\odot$) protostars with cold mass accretion.

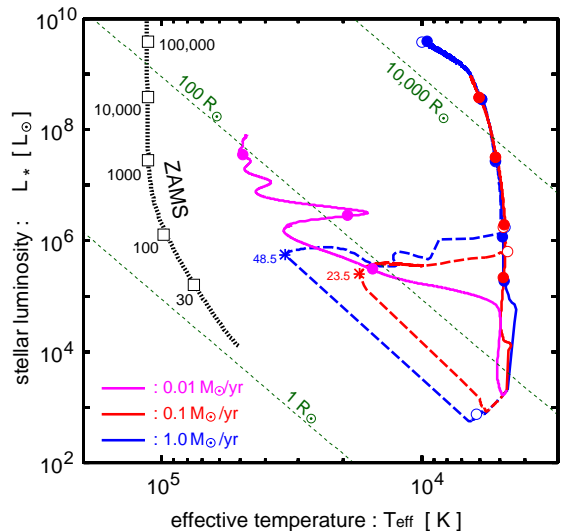


FIG. 8.— Evolutionary tracks in the HR diagram. The different colors represent the accretion rates $1.0 M_\odot \text{ yr}^{-1}$ (blue), $0.1 M_\odot \text{ yr}^{-1}$ (red), and $0.01 M_\odot \text{ yr}^{-1}$ (magenta). Only the cases with $\eta = 0.1$ (cases a1-e0.1, a0.1-e0.1, and a0.01-e0.1) and $\eta = 0$ (cases a1-e0 and a0.1-e0) are presented. The asterisks on the dashed lines mark the points where the effective temperature takes the highest value for $\eta = 0$. The stellar masses at these points are also labeled. The black dotted line represents the loci of non-accreting zero metallicity ZAMS stars. The circles and squares on the tracks represent positions of $30 M_\odot$, $100 M_\odot$, $1000 M_\odot$, $10^4 M_\odot$, and $10^5 M_\odot$ stars in ascending order. Stellar radii at constant values $10^4 R_\odot$, $100 R_\odot$, and $1 R_\odot$ are shown by thin green dashed lines.

3.1.5. Evolution in the HR Diagram

Figure 8 shows the evolutionary tracks in the Hertzsprung-Russell diagram for several representative cases. As shown in HOY12 for cases with rapid mass accretion $\dot{M}_* \geq 0.1 M_\odot$, the tracks are almost vertical as the stellar mass, luminosity and radius increase for $M_* \gtrsim 100 M_\odot$. The tracks for $\dot{M}_* = 1.0 M_\odot$ show a gradual increase of the effective temperature for $M_* \gtrsim 10^4 M_\odot$, finally reaching $\simeq 10^4$ K at $M_* = 10^5 M_\odot$ (see Figure 1). Only during the early phases before the stellar mass (luminosity) exceeds $100 M_\odot$ ($10^6 L_\odot$), does the effective temperature depend on the input energy fraction η , i.e. lower η results in higher effective temperature. The evolutionary track for $\dot{M}_* = 10^{-2} M_\odot \text{ yr}^{-1}$ lies between the above tracks and the ZAMS line. Despite the apparent differences among these tracks, the stellar luminosities for a given mass are nearly the same in all cases for $M_* \gtrsim 1000 M_\odot$, namely the Eddington value. It is clear that SMSs with extremely high mass accretion rates will have low effective temperatures compared to non-accreting or slowly accreting SMSs. This fact has a number of consequences on star and BH formation in the early universe, as discussed in Sec. 4 below.

3.2. Stellar Pulsational Instability

Next we study the pulsation stability of accreting SMSs and estimate the resulting mass-loss rates for unstable cases. Following our previous work (IHO13; Inayoshi et al. 2013b), we apply linear stability analysis to the stellar models with different masses. IHO13 show that an SMS is more unstable with higher accretion rates

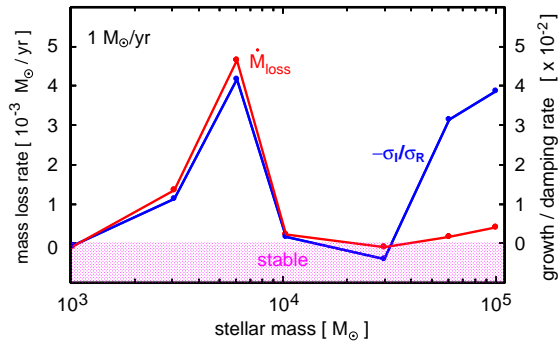


FIG. 9.— The pulsation stability of an accreting SMS at the rate $\dot{M}_* = 1.0 M_\odot \text{ yr}^{-1}$ (case a1-e0.1). The growth/damping rates of the stellar pulsation ($-\sigma_I/\sigma_R$) and the resulting mass-loss rates (\dot{M}_{loss}) are plotted as a function of the stellar mass. In the shaded region, the star is stable against the stellar pulsation.

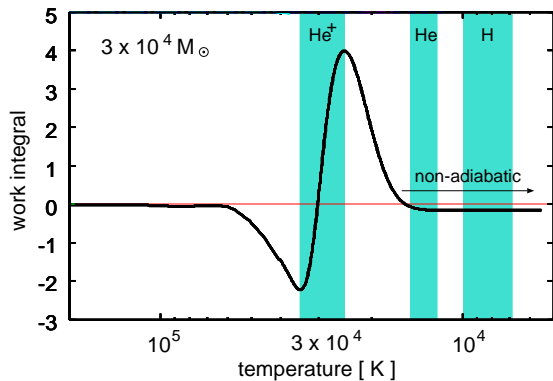


FIG. 10.— The work integral (in arbitrary units, see text) for a $3 \times 10^4 M_\odot$ star accreting at the rate $\dot{M}_* = 1.0 M_\odot \text{ yr}^{-1}$ (case a1-e0.1). Only the distribution near the stellar surface is presented as a function of the interior temperature. The shaded backgrounds represent the ionization layers of He^+ , He, and H. The outermost part is the non-adiabatic layer, where the pulsation instability is not excited because of radiative diffusion.

and at higher stellar masses. We thus focus on the case with the highest accretion rate $\dot{M}_* = 1.0 M_\odot \text{ yr}^{-1}$ for examining whether the mass loss caused by the stellar pulsation can limit stellar growth via mass accretion. Since accreting SMSs are most unstable against radial perturbations for $M_* \lesssim 10^3 M_\odot$ (IHO13), we also analyze the stability against radial perturbations. Our current results allow us to extend the analysis to the high mass range of $10^3 M_\odot \leq M_* \leq 10^5 M_\odot$.

The basic procedure of our linear stability analysis is briefly summarized as follows (see Appendix in IHO13 for more details). First, we linearize the four *time-dependent* stellar structure equations (i.e., the continuity, momentum, energy, and energy transfer equations) and the Poisson equation, applying radial perturbations to the physical quantities. We here consider the perturbations proportional to $e^{i\sigma t}$, where $\sigma = \sigma_R + i\sigma_I$, and σ_R and $|\sigma_I|$ are the frequency and growth (or damping) rate of the pulsation. For instance, one of the perturbed quantities is the radial displacement of a fluid element from the equilibrium position, $\xi(r, t) \equiv \xi_r(r)e^{i\sigma t}$. Retaining first order results in a system of ordinary derivative equations for

the perturbed quantities (e.g., $\xi_r(r)$) and σ . We solve these equations with appropriate boundary conditions, finding solutions for particular eigenvalues of σ . The radial profiles of the perturbations are given as the eigenfunctions of this system of equations.

Figure 9 shows the evolution of the growth/damping rates of pulsation as a function of the accreted mass. The mass-loss rates are estimated assuming that all the pulsation energy is converted into kinetic energy of the outflowing gas:

$$\frac{\dot{M}_{\text{loss}}}{2} v_{\text{esc}}^2 = 2|\sigma_I|E_W, \quad (9)$$

where $v_{\text{esc}} = (2GM_*/R_*)^{1/2}$ is the escape velocity from the stellar surface,

$$E_W = \frac{\sigma_R^2}{2} \int_0^{M_*} |\xi_r|^2 dM_r, \quad (10)$$

is the pulsation energy, and M_r the enclosed mass. Since pulsation energy is partially lost through radiative dissipation, our estimate of the mass-loss rate should be considered an upper limit (Papaloizou 1973a,b).

In agreement with our previous analysis we find that the instability is excited by the κ mechanism due to the opacity bump in the He^+ ionization layer. The accreting SMS is always unstable, except within the narrow mass range $10^4 M_\odot \lesssim M_* \lesssim 3 \times 10^4 M_\odot$. The mass-loss rate rises with increasing mass for $M_* \lesssim 6 \times 10^3 M_\odot$. The derived mass-loss rate at $M_* \sim 10^3 M_\odot$ is somewhat lower than the value shown in IHO13, which we attribute to the different numerical code employed in this paper. The current stellar model has a slightly higher temperature in the surface layers than the model analyzed in IOH13. The layers with the opacity bump, where the pulsation is excited, contains a smaller fraction of the stellar mass, which results in a lower mass-loss rate. The maximum mass-loss rate is $5 \times 10^{-3} M_\odot \text{ yr}^{-1}$ at $M_* \simeq 6 \times 10^3 M_\odot$. After this the mass-loss rate hardly rises in spite of the growth rate increasing with stellar mass. This is primarily because the escape velocity increases with stellar mass (see eq. 9), as the stellar expansion slows down for $M_* \gtrsim 10^4 M_\odot$ (Fig. 1-a). Since the mass-loss rates are much lower than the assumed accretion rate, we conclude that the pulsation instability does not prevent the formation of an SMS via rapid mass accretion.

When the stellar mass exceeds $6 \times 10^3 M_\odot$, the pulsation is stabilized and the pulsation-driven outflows are also suppressed. To understand this stabilization, we consider the work integral defined by

$$W(M_r) = \frac{\pi}{\sigma_R} \int_0^{M_r} \Re \left[\frac{\delta T^*}{T} \left(\delta \epsilon - \frac{d}{dM_r} \delta L_{\text{rad}} \right) \right] dM_r, \quad (11)$$

where ϵ is the nuclear energy production rate per unit mass, L_{rad} the radiative luminosity, the symbols with δ represent the Lagrange perturbations, and $\Re[\]$ denotes taking the real part of a quantity. The work integral physically represents the pulsation energy gained during one period within the mass coordinate M_r . The stellar pulsation is excited (damped) in the layer where dW/dM_r is positive (negative). If the work integral at the stellar surface $W(M_*)$ is positive (negative), the protostar is unstable (stable).

Figure 10 shows the radial profile of the work integral near the surface of a $3 \times 10^4 M_\odot$ star. We see that the work integral increases outward within the He^+ ionization layer, but decreases beyond it because of radiative diffusion. In the outermost layers with $T \lesssim 18000$ K, where the radiative cooling time is shorter than the pulsation period, the work integral remains constant without excitation or damping (so-called the *non-adiabatic region*). In this case, the work integral at the stellar surface is negative and the protostar is stable. In the most unstable case when $M_* = 6 \times 10^3 M_\odot$, on the other hand, radiative cooling in the outermost part is more efficient and the non-adiabatic region extends further inward. The transition point to the non-adiabatic region is located just outside of the He^+ ionization layer. Therefore, the stellar pulsation excited in the He^+ ionization layer does not suffer from damping via radiative diffusion outside the ionization layer. Such a profile of the work integral is displayed in Figure 3 of IHO13, where by simply extrapolating the available results for $M_* < 10^3 M_\odot$ without considering the damping effect outside the He^+ ionization layer, we had speculated that the mass-loss rates would increase with stellar mass for $M_* > 10^3 M_\odot$. By contrast, our current results show that the pulsation instability is strongly suppressed for $M_* \gg 10^3 M_\odot$ and mass-loss is much lower than predicted by IHO13.

Note that the pulsational instability considered above qualitatively differs from that of non-accreting massive primordial stars, which is caused by the ϵ -mechanism (e.g., Baraffe et al. 2001; Sonoi & Umeda 2012). The pulsation driven by the ϵ -mechanism could work when a SMS contracts and approaches the ZAMS stage after the mass accretion ceases (also see Sec. 4.3).

4. DISCUSSION

4.1. UV feedback from Rapidly Accreting Supermassive Stars

As mentioned in Sec. 1, for a more typical case of primordial star formation, stellar UV feedback becomes so strong that it is able to shut off the mass accretion onto the star (e.g., Hosokawa et al. 2011b, 2012b). By contrast, the stellar evolution calculations presented here predict that this is not the case when forming primordial SMSs via very rapid mass accretion. Figure 11 shows that with extremely high accretion rates $\dot{M}_* \geq 0.1 M_\odot \text{ yr}^{-1}$, the stellar output of hydrogen-ionizing photons remains very low even after the stellar mass exceeds $10^4 M_\odot$. For accretion at $1.0 M_\odot \text{ yr}^{-1}$ the hydrogen-ionizing luminosity for $M_* \simeq 10^5 M_\odot$ is still comparable to that of $M_* \lesssim 100 M_\odot$ primordial ZAMS stars. This is a consequence of the low effective temperature resulting from the large stellar radius. For $\dot{M}_* = 0.1 M_\odot \text{ yr}^{-1}$, the accretion rate of hydrogen atoms is $\simeq 3 \times 10^{49} \text{ sec}^{-1}$. An HII region cannot grow if the stellar hydrogen-ionizing photon emissivity is lower than this hydrogen accretion rate. Only for the extreme cases with low-entropy accretion $\eta = 0$, would the ionizing luminosity temporarily increase in an early stage when $M_* < 100 M_\odot$, visible as a spike in Figure 11. This occurs shortly before the abrupt expansion of the star (Figs. 6 and 7), when the stellar total luminosity also sharply rises. Even if this “flash” of ionizing radiation would occur, however, its duration of < 100 years is too

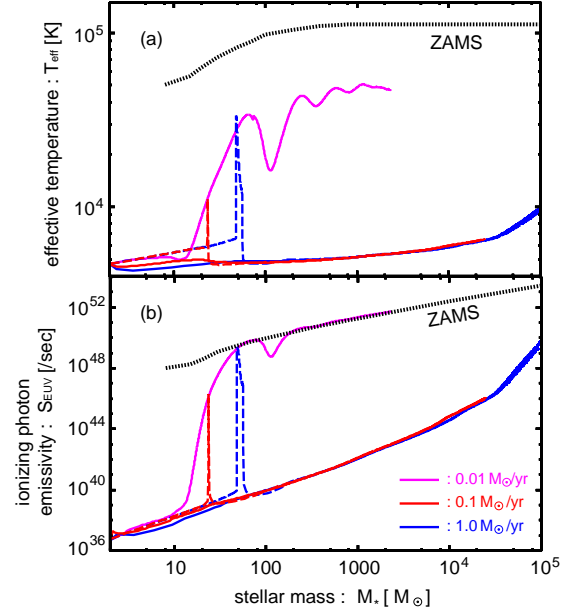


FIG. 11.— Evolution of the stellar effective temperature (*upper panel*) and ionizing photon emissivity (*lower panel*). The lines represent the same cases as in Figure 8. The black dotted line presents the values of ZAMS stars.

short to significantly disturb the accretion flow. It is thus unlikely that the mass accretion onto rapidly accreting SMSs is hindered by stellar UV feedback, at least for $M_* \lesssim 10^5 M_\odot$.

After the stellar mass exceeds $10^5 M_\odot$, however, the stellar ionizing flux will continue to increase, so that an HII region might finally emerge. The UV feedback caused by the dynamical expansion of the HII region would shut off the mass accretion as expected in the ordinary cases of the primordial star formation (e.g., McKee & Tan 2008; Hosokawa et al. 2011b). The maximum stellar mass by the UV feedback would be higher with more rapid mass accretion, as suggested in our radiation hydrodynamic numerical simulations (Hosokawa et al. 2011b, 2012b).

By contrast, stellar UV feedback at a lower accretion rate $\dot{M}_* = 10^{-2} M_\odot \text{ yr}^{-1}$ will slow and perhaps stop the accretion flow. Although this rate is too low to form an SMS, such moderately rapid accretion can be expected occasionally in the ordinary mode of primordial star formation (e.g., Hirano et al. 2013). Figures 8 and 11-(a) show that, in this case, the effective temperature always lies between the ZAMS and the rapidly-accreting ($\dot{M}_* \geq 0.1 M_\odot \text{ yr}^{-1}$) values. However, Figure 11-(b) shows that the evolution of the stellar ionizing luminosity is almost the same as in the ZAMS case. This is because the larger radius (Fig. 6-b) compensates for the lower effective temperature, resulting in a comparable UV luminosity. Although stellar UV feedback is certainly expected in this case, it is somewhat weaker than for the ZAMS stars because of the lower average energy of ionizing photons.

4.2. Observational Detectability

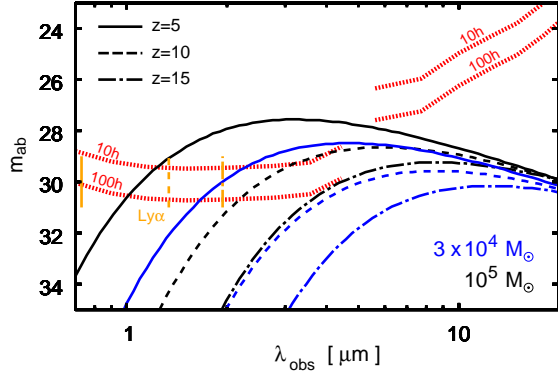


FIG. 12.— Apparent AB magnitudes of bloated supermassive stars and detection limits of the James Webb Telescope (JWST). The black and blue lines represent the $3 \times 10^4 M_\odot$ and $10^5 M_\odot$ stars located at redshifts $z = 5$ (solid), 10 (dashed), and 15 (dot-solid lines). The bolometric luminosities of these stars are $1.1 \times 10^9 L_\odot$ and $3.8 \times 10^9 L_\odot$ respectively. The red dotted lines show the JWST 10σ detection limits with the exposure times of 10 and 100 hours using the Near Infrared Camera (NIRCam, left) and Mid-Infrared Camera (MIRI, right). The JWST photometric sensitivity data are taken from the web site, <http://www.stsci.edu/jwst/science/sensitivity/jwst-phot>. The orange vertical lines mark the wavelength of Ly- α line at each redshift, indicating that intergalactic absorption would reduce the original spectrum for the wavelengths shorter than this point.

Although the UV luminosity of an accreting SMS is much weaker than its ZAMS counterpart, the bolometric luminosity could exceed $10^9 L_\odot$, increasing with stellar mass almost linearly. With such a high luminosity individual SMSs could be detectable with future observational facilities such as the James Webb Space Telescope (JWST). Figure 12 demonstrates this, showing that bloated SMSs at $z \sim 10$ are detectable by JWST with exposure times of 10 to 100 hours. The cosmological parameters for the standard Λ CDM (Komatsu et al. 2011) and black-body spectrum with the effective temperature T_{eff} are adopted here.

Actually, the observational features of accreting SMSs are very similar to those of hypothetical supermassive dark stars (SMDSSs), which are powered by energy production via annihilation of dark matter (DM) rather than nuclear fusion (e.g., Spolyar et al. 2008; Umeda et al. 2009). This is because SMDSSs could have a very large radius $R_* \gtrsim 10$ AU and a low effective temperature $T_{\text{eff}} \lesssim 10^4$ K, similar to the accreting SMSs presented in this paper. Recent studies that examined the observational signatures and detectability of SMDSSs (e.g., Zackrisson et al. 2010; Freese et al. 2010; Ilie et al. 2012), are thus applicable to accreting SMSs as well. For instance, SMDSS and SMS colors obtained from multi-band survey data should be unusual compared to ordinary galaxies and AGNs because of their very low effective temperature (Zackrisson et al. 2010). Note that the evolution and apparent colors of SMDSSs are strongly dependent on supply rates of annihilating DM (Freese et al. 2010). Once the SMDSSs are no longer supplied with sufficient DM, they contract, increasing their effective temperature. It is thus only in extreme cases that a $10^5 M_\odot$ SMDSS would still have a low effective temperature of $T_{\text{eff}} \lesssim 10^4$ K. By contrast, rapid mass accretion keeps SMSs inflated, resulting in a low T_{eff} without DM annihilation. The brightest sources with unusually red colors

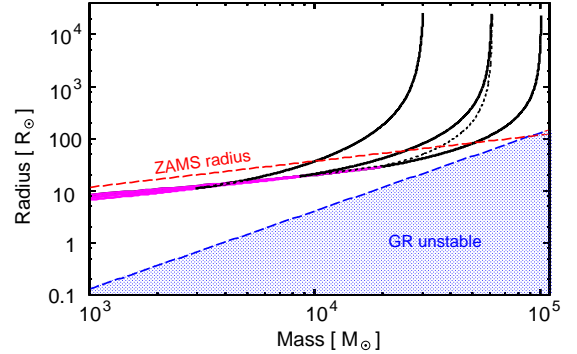


FIG. 13.— General-relativistic stability of supermassive stars growing via very rapid mass accretion. The solid curves depict the radial mass distributions in the interior of the $3 \times 10^4 M_\odot$, $6 \times 10^4 M_\odot$, and $10^5 M_\odot$ stars in case a1-e0.1, i.e., with $\dot{M}_* = 1.0 M_\odot \text{ yr}^{-1}$ and $\eta = 0.1$. The dotted curve presents the same profile of $6 \times 10^4 M_\odot$ star but for the lower accretion rate $0.3 M_\odot \text{ yr}^{-1}$ (case a0.3-e0.1). The magenta parts of these curves denote the central convective core. The red dashed line represents the mass-radius relation of primordial ZAMS stars (Johnson et al. 2013c). The blue dashed line represents the critical radii of the GR stability for $n = 3$ polytrope stars (Fricke 1973), below which the stellar structure is unstable. Note that the horizontal axis denotes the mass coordinate for the solid and dotted curves and the stellar mass for the dashed lines.

might be a signature of rapidly accreting SMSs rather than of SMDSSs.

The detection rate of accreting SMSs depends on their formation rate per unit redshift and typical lifetime. Agarwal et al. (2012) and Johnson et al. (2013a) show that the formation of the SMSs via rapid mass accretion should be more ubiquitous than previously thought. They show that, within the lifetime of 10^6 yr, at least a few accreting SMSs should lie in the survey area of $\sim 100 \text{ arcmin}^2$. The exact lifetime of a SMS depends on the final stage of its evolution, which is affected by the mass accretion history (also see Sec. 4.3).

4.3. The Ultimate Fate of Accreting Supermassive Stars

Our results suggest that rapid mass accretion onto SMSs drastically changes their stellar structure, causing significant bloating. This could also influence their ultimate fate. As described in Sec. 1, SMSs exceeding $10^5 M_\odot$ are thought to directly collapse to form massive BHs via a GR instability. However, previous studies assume that the SMSs are polytropic stars with index $n = 3$, i.e., fully convective stars with homogeneous entropy distributions. Our calculations show that this is not the case for rapid mass accretion. As Figure 3-(a) shows, in the stellar interior, the specific entropy increases outward until reaching the surface convective layer. The homogeneous convective core gradually extends after hydrogen burning is ignited at the stellar center.

Whereas GR effects are not taken into account in the current calculations, we have also performed a few test runs with a gravitational constant G_{eff} modified by post-Newton corrections

$$G_{\text{eff}} = G \left(1 + \frac{P}{\rho c^2} + \frac{4\pi r^3 P}{M c^2} + \frac{2GM}{c^2 r} \right) \quad (12)$$

(e.g., Fuller et al. 1986) and see no significant differences from the results presented above. This is demonstrated in Figure 13, which shows the stability of SMSs accreting at the rates $\dot{M}_* = 1.0 M_\odot \text{ yr}^{-1}$ and $0.3 M_\odot \text{ yr}^{-1}$. The SMSs are still stable as far as we have followed their evolution. Note that, although the entire stellar structure is not well approximated by a $n = 3$ polytrope, the unstable area in the figure is applicable to the central convective core.

Extrapolating the current results, we expect that the star becomes unstable when the stellar mass reaches a few $\times 10^5 M_\odot$ for $\dot{M}_* = 1.0 M_\odot \text{ yr}^{-1}$. We expect that not the entire star but only its inner core might collapse due to the GR instability. This is because the outer part broadly extends with high specific entropy obtained with very rapid mass accretion. If a BH forms as a result of the collapse, an accretion disk should also form and grow as the surrounding gas falls toward the center. A quasi-star powered by the energy production in the accretion disk instead of nuclear fusion (Begelman et al. 2008) might finally emerge. The figure also suggests that the GR instability could work for a slightly lower mass assuming a lower accretion rate, because the mass distribution in the interior is more centrally condensed (also see Sec. 3.1.2). With significantly lower accretion rates $\dot{M}_* \lesssim 0.1 M_\odot \text{ yr}^{-1}$, however, the star would exhaust its nuclear fuel and collapse directly to a BH before the GR instability sets in.

Note that the above scenario assumes ongoing mass accretion when the GR instability sets in. As discussed in Sec. 4.1, however, stellar UV feedback might halt the mass accretion before the GR instability sets in. Without mass accretion, the bloated SMS should contract on a KH timescale and finally become a ZAMS star, which has a homogeneous entropy distribution because of efficient convective mixing. For such $n \simeq 3$ polytrope stars, the GR instability should cause most of the stellar matter to collapse to a massive BH (e.g., Fricke 1973; Fuller et al. 1986). In this case, the stellar lifetime might be somewhat longer than in the above case, where the SMS collapses before the mass accretion ceases.

Even if a part of the star becomes unstable, this does not necessarily mean that a BH forms from the collapse. It is conceivable that a very energetic supernova explosion results from runaway nuclear fusion. Although this is less likely with the lower metallicities (e.g., Montero et al. 2012), recent studies suggest that this might occur in the early universe (e.g., Whalen et al. 2012; Johnson et al. 2013b). Moreover, the evolution of an SMS should also depend on other parameters, e.g., the interior rotation and magnetic fields. Indeed, Yoon et al. (2012) show that the ultimate fates of $M_* \leq 10^3 M_\odot$ primordial stars vary with these parameters. The dynamics of the final collapse should also depend on the stellar rotation. Reisswig et al. (2013) show that a massive binary BH might form through the collapse of a rapidly rotating SMS. Thus, the final fates of SMSs should be studied further under consideration of all the potential effects of very rapid mass accretion, truncation of accretion, runaway nuclear fusion, the GR instability, and stellar rotation and magnetic fields.

4.4. Seeding Supermassive Black Holes with Supermassive Stars

Besides following the evolution of individual accreting SMSs and the resulting formation of massive BHs, it is also important to consider how often this occurs in the early universe. As described in Sec. 1, SMSs should form in massive dark halos where H_2 molecules are destroyed. Previous studies have mostly considered that H_2 molecules are destroyed by photodissociating radiation from neighboring stars, showing that the environments for forming the SMSs are extremely rare (e.g., Dijkstra et al. 2008). Regarding this issue, Agarwal et al. (2012) demonstrate that the occurrence rate of SMS formation should be elevated when considering the soft UV radiation from Pop II stars, and that the number density of massive BHs at $z \gtrsim 6$ expected from current observations (e.g., Treister et al. 2011; Mortlock et al. 2011) could agree with this scenario. However, it is still uncertain whether H_2 photodissociation is the dominant process which causes the SMS formation or not. Inayoshi & Omukai (2012), for instance, show that H_2 molecules are easily collisionally dissociated in dense shocks emerging in colliding cold accretion flows at the galaxy formation epoch. This could be more common than the strong photodissociating radiation field and should be examined in detail in future studies.

Recent numerical simulations are beginning to reveal the dynamical evolution in an early stage of SMS formation, whereby a massive circumstellar disk forms as gas falls toward the center of a gas cloud (e.g., Regan & Haehnelt 2009; Latif et al. 2013a; Choi et al. 2013). However, several assumptions of the simulations are somewhat arbitrary for enabling SMS formation, e.g., turning off H_2 molecular cooling or elevating the photodissociating background field by hand. We need more realistic simulations beginning with the initial conditions naturally provided by modern cosmology.

These previous simulations do not show that a SMS with $M_* \gg 1000 M_\odot$ actually forms via rapid mass accretion. We have shown, for the first time, the formation of a $M_* \simeq 10^5 M_\odot$ SMS with the large accretion rates predicted by previous studies. Our results also suggest that stellar radiative feedback could be effective after the stellar mass exceeds $10^5 M_\odot$, a prediction which needs to be examined with more detailed simulations. It would be necessary to consistently follow the growth of the supergiant protostar and the evolution of the accretion flow, by including stellar radiative feedback (e.g., Hosokawa et al. 2011b).

5. CONCLUSIONS

In this paper, we have studied the evolution of rapidly accreting SMSs, which could be the precursors of SMBHs observed at $z \gtrsim 6$. To this end, extending our previous work HOY12, we have followed the evolution until the stellar mass reaches $10^{4-5} M_\odot$ by numerically solving the stellar interior structure taking account of the effects of the rapid mass accretion.

In order to avoid numerical convergence difficulties which limited the calculations for $M_* \lesssim 10^3 M_\odot$ in HOY12, we have employed a different stellar evolution code in this paper (Yorke & Bodenheimer 2008).

The current calculations agree with our previous results, showing that a rapidly accreting SMS forms through the supergiant-protostar stage. The stellar radius monotonically increases as the stellar mass increases, obeying the analytic mass-radius relation (1). The stellar interior is very inhomogeneous during this stage; most of the interior contracts radiating the energy away, whereas a surface layer containing a small fraction of the stellar mass inflates. The stellar expansion continues even after the stellar mass exceeds $10^3 M_\odot$, until the radius finally begins to slightly decrease for $\gtrsim 3 \times 10^4 M_\odot$. The termination of the expansion is inevitable, because H^- bound-free opacity, which keeps the stellar effective temperature locked at $\simeq 5000$ K, becomes unavailable as the density in the stellar surface layers drops below $10^{-11} \text{ g cm}^{-3}$. Nonetheless, the stellar radius remains very large, $R_* \simeq 2 \times 10^4 R_\odot \simeq 100 \text{ AU}$ for $M_* \gtrsim 10^4 M_\odot$, as long as the rapid mass accretion continues.

Our current results suggest that SMSs initially form as very bloated supergiant stars. With this very large radius, the stellar effective temperature is less than 10^4 K even after the protostar becomes supermassive. Stellar UV radiation is much weaker than for non-accreting ZAMS stars. For instance, the ionizing luminosity of a rapidly accreting $10^5 M_\odot$ star should be less than that of a $100 M_\odot$ ZAMS star. Strong UV feedback, which could limit the mass accretion onto the star, is thus unlikely to operate in this case. We have also studied the pulsation stability of accreting SMSs with our calculated stellar models. Our analyses show that accreting SMSs become pulsation unstable due to the κ -mechanism (IHO13), but the resulting mass-loss rates are still much lower than the accretion rates for $M_* \gtrsim 10^3 M_\odot$. Therefore, we conclude that the SMSs formed via very rapid mass accretion are not significantly affected by stellar UV feedback or pulsational mass loss. Once a star becomes supermassive, the stellar bolometric luminosity could exceed

$10^9 L_\odot$. Rapidly accreting SMSs are thus in principle detectable with future observational facilities like JWST.

The evolution after the birth of the SMSs is critical for understanding the origins of the SMBHs in the early universe. Our calculations show that only the inner core of an accreting SMS could become GR unstable as the stellar mass increases. Extrapolating the current results with the accretion rate of $1.0 M_\odot \text{ yr}^{-1}$, for instance, we expect that the star would suffer from the GR instability when the stellar mass reaches a few $\times 10^5 M_\odot$. The subsequent evolution is beyond the scope of our current study. If a BH forms after the inner part of the star gravitationally collapses, a so-called quasi-star (Begelman et al. 2008) might emerge. However, it is also possible that an energetic supernova explosion occurs with run-away nuclear fusion during the collapse. Moreover, as the effective temperature gradually increases, stellar UV feedback could eventually halt mass accretion for $M_* \gtrsim 10^5 M_\odot$, if the emission of hydrogen-ionizing photons significantly exceeds the infall rate of hydrogen atoms. If mass accretion stops, the SMS would contract on a KH timescale. The GR instability could set in as the SMS approaches the ZAMS stage. The above scenario depends on the late stages of SMS evolution, which should be investigated further in future studies.

The authors thank Hideyuki Umeda, Yuichiro Sekiguchi, Neal Turner, Dominik Schleicher, and Francesco Palla for fruitful discussions and comments. T.H. appreciates the support by Fellowship of the Japan Society for the Promotion of Science for Research Abroad. K.I., K.O., and N.Y. are supported by the Grants-in-Aid by the Ministry of Education, Science and Culture of Japan (23-838, 2168407, 21244021, and 25287050). Portions of this work were conducted at the Jet Propulsion Laboratory, California Institute of Technology, operating under a contract with the National Aeronautics and Space Administration (NASA).

REFERENCES

- Agarwal, B., Khochfar, S., Johnson, J. L., Neistein, E., Dalla Vecchia, C., & Livio, M. 2012, *MNRAS*, 425, 2854
- Appenzeller, I., & Fricke, K. 1972a, *A&A*, 18, 10
- . 1972b, *A&A*, 21, 285
- Baraffe, I., Heger, A., & Woosley, S. E. 2001, *ApJ*, 550, 890
- Begelman, M. C. 2010, *MNRAS*, 402, 673
- Begelman, M. C., Rossi, E. M., & Armitage, P. J. 2008, *MNRAS*, 387, 1649
- Bodenheimer, P., Laughlin, G. P., Różyczka, M., & Yorke, H. W., eds. 2007, *Numerical Methods in Astrophysics: An Introduction*
- Bromm, V., & Loeb, A. 2003, *ApJ*, 596, 34
- Bromm, V., Yoshida, N., Hernquist, L., & McKee, C. F. 2009, *Nature*, 459, 49
- Chandrasekhar, S. 1964, *Physical Review Letters*, 12, 114
- Choi, J.-H., Shlosman, I., & Begelman, M. C. 2013, *ApJ*, 774, 149
- Dijkstra, M., Haiman, Z., Mesinger, A., & Wyithe, J. S. B. 2008, *MNRAS*, 391, 1961
- Freese, K., Ilie, C., Spolyar, D., Valluri, M., & Bodenheimer, P. 2010, *ApJ*, 716, 1397
- Fricke, K. J. 1973, *ApJ*, 183, 941
- Fuller, G. M., Woosley, S. E., & Weaver, T. A. 1986, *ApJ*, 307, 675
- Haiman, Z. 2013, in *Astrophysics and Space Science Library*, Vol. 396, *Astrophysics and Space Science Library*, ed. T. Wiklund, B. Mobasher, & V. Bromm, 293
- Hartmann, L., Cassen, P., & Kenyon, S. J. 1997, *ApJ*, 475, 770
- Hayashi, C. 1961, *PASJ*, 13, 450
- Heney, L. G., Forbes, J. E., & Gould, N. L. 1964, *ApJ*, 139, 306
- Hirano, S., Hosokawa, T., Yoshida, N., Umeda, H., Omukai, K., Chiaki, G., & Yorke, H. W. 2013, *ArXiv e-prints*:1308.4456
- Hosokawa, T., Offner, S. S. R., & Krumholz, M. R. 2011a, *ApJ*, 738, 140
- Hosokawa, T., & Omukai, K. 2009, *ApJ*, 691, 823
- Hosokawa, T., Omukai, K., & Yorke, H. W. 2012a, *ApJ*, 756, 93
- Hosokawa, T., Omukai, K., Yoshida, N., & Yorke, H. W. 2011b, *Science*, 334, 1250
- Hosokawa, T., Yorke, H. W., & Omukai, K. 2010, *ApJ*, 721, 478
- Hosokawa, T., Yoshida, N., Omukai, K., & Yorke, H. W. 2012b, *ApJ*, 760, L37
- Iben, Jr., I. 1963, *ApJ*, 138, 1090
- Ilie, C., Freese, K., Valluri, M., Iliev, I. T., & Shapiro, P. R. 2012, *MNRAS*, 422, 2164
- Inayoshi, K., Hosokawa, T., & Omukai, K. 2013a, *MNRAS*, 431, 3036
- Inayoshi, K., & Omukai, K. 2011, *MNRAS*, 416, 2748
- . 2012, *MNRAS*, 422, 2539
- Inayoshi, K., Sugiyama, K., Hosokawa, T., Motogi, K., & Tanaka, K. E. I. 2013b, *ApJ*, 769, L20
- Johnson, J. L., Dalla, V. C., & Khochfar, S. 2013a, *MNRAS*, 428, 1857
- Johnson, J. L., Whalen, D. J., Even, W., Fryer, C. L., Heger, A., Smidt, J., & Chen, K.-J. 2013b, *ApJ*, 775, 107
- Johnson, J. L., Whalen, D. J., Fryer, C. L., & Li, H. 2012, *ApJ*, 750, 66
- Johnson, J. L., Whalen, D. J., Li, H., & Holz, D. E. 2013c, *ApJ*, 771, 116
- Kippenhahn, R., & Meyer-Hofmeister, E. 1977, *A&A*, 54, 539

- Kippenhahn, R., Weigert, A., & Weiss, A. 2013, *Stellar Structure and Evolution: Astronomy and Astrophysics Library*. ISBN 978-3-642-30255-8. Springer-Verlag Berlin Heidelberg, 2013
- Komatsu, E., et al. 2011, *ApJS*, 192, 18
- Latif, M. A., Schleicher, D. R. G., Schmidt, W., & Niemeyer, J. 2013a, *MNRAS*, 433, 1607
- Latif, M. A., Schleicher, D. R. G., Schmidt, W., & Niemeyer, J. C. 2013b, *ArXiv e-prints*:1309.1097
- Mayer, M., & Duschl, W. J. 2005, *MNRAS*, 358, 614
- McKee, C. F., & Tan, J. C. 2008, *ApJ*, 681, 771
- Montero, P. J., Janka, H.-T., & Müller, E. 2012, *ApJ*, 749, 37
- Mortlock, D. J., et al. 2011, *Nature*, 474, 616
- Oh, S. P., & Haiman, Z. 2002, *ApJ*, 569, 558
- Omukai, K. 2001, *ApJ*, 546, 635
- Omukai, K., & Palla, F. 2001, *ApJ*, 561, L55
- . 2003, *ApJ*, 589, 677
- Omukai, K., Schneider, R., & Haiman, Z. 2008, *ApJ*, 686, 801
- Osaki, Y. 1966, *PASJ*, 18, 384
- Palla, F., & Stahler, S. W. 1992, *ApJ*, 392, 667
- Papaloizou, J. C. B. 1973a, *MNRAS*, 162, 143
- . 1973b, *MNRAS*, 162, 169
- Regan, J. A., & Haehnelt, M. G. 2009, *MNRAS*, 393, 858
- Reisswig, C., Ott, C. D., Abdikamalov, E., Haas, R., Moesta, P., & Schnetter, E. 2013, *ArXiv e-prints*:1304.7787
- Schleicher, D. R. G., Palla, F., Ferrara, A., Galli, D., & Latif, M. 2013, *ArXiv e-prints*:1305.5923
- Shang, C., Bryan, G. L., & Haiman, Z. 2010, *MNRAS*, 402, 1249
- Shibata, M., & Shapiro, S. L. 2002, *ApJ*, 572, L39
- Siess, L., & Forestini, M. 1996, *A&A*, 308, 472
- Siess, L., Forestini, M., & Bertout, C. 1997, *A&A*, 326, 1001
- Sonoi, T., & Umeda, H. 2012, *MNRAS*, 421, L34
- Spolyar, D., Freese, K., & Gondolo, P. 2008, *Physical Review Letters*, 100, 051101
- Stacy, A., Greif, T. H., & Bromm, V. 2010, *MNRAS*, 403, 45
- . 2012, *MNRAS*, 2508
- Stahler, S. W., Palla, F., & Salpeter, E. E. 1986, *ApJ*, 302, 590
- Stahler, S. W., Shu, F. H., & Taam, R. E. 1980, *ApJ*, 241, 637
- Susa, H. 2013, *ApJ*, 773, 185
- Treister, E., Schawinski, K., Volonteri, M., Natarajan, P., & Gawiser, E. 2011, *Nature*, 474, 356
- Umeda, H., Yoshida, N., Nomoto, K., Tsuruta, S., Sasaki, M., & Ohkubo, T. 2009, *J. Cosmol. Astropart. Phys.*, 8, 24
- Unno, W. 1971, *PASJ*, 23, 123
- Whalen, D. J., Heger, A., Chen, K.-J., Even, W., Fryer, C. L., Stiaivelli, M., Xu, H., & Joggerst, C. C. 2012, *ArXiv e-prints*:1211.1815
- Whalen, D. J., Johnson, J. L., Smidt, J., Heger, A., Even, W., & Fryer, C. L. 2013a, *ArXiv e-prints*:1308.3278
- Whalen, D. J., Johnson, J. L., Smidt, J., Meiksin, A., Heger, A., Even, W., & Fryer, C. L. 2013b, *ApJ*, 774, 64
- Wise, J. H., Turk, M. J., & Abel, T. 2008, *ApJ*, 682, 745
- Wolcott-Green, J., Haiman, Z., & Bryan, G. L. 2011, *MNRAS*, 418, 838
- Yoon, S.-C., Dierks, A., & Langer, N. 2012, *A&A*, 542, A113
- Yorke, H. W., & Bodenheimer, P. 2008, in *Astronomical Society of the Pacific Conference Series*, Vol. 387, *Massive Star Formation: Observations Confront Theory*, ed. H. Beuther, H. Linz, & T. Henning, 189
- Zackrisson, E., et al. 2010, *ApJ*, 717, 257
- Zinnecker, H., & Yorke, H. W. 2007, *ARA&A*, 45, 481